THE JOURNAL OF PHYSICAL CHEMISTRY C
A JOURNAL OF THE AMERICAN CHEMICAL SOCIETY

Open Access
This article is licensed under CC-BY 4.0

pubs.acs.org/JPCC
Article

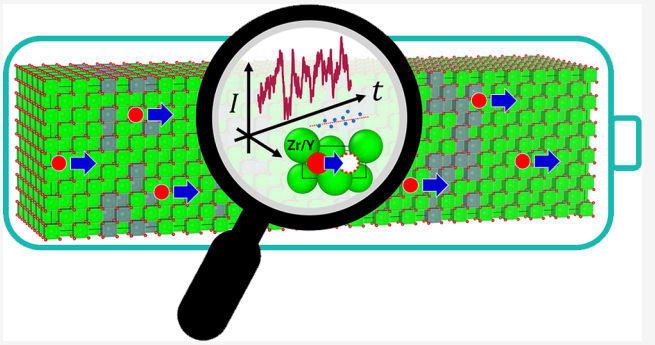
Linking Microscopic Structures to Ionic Currents in Solid Electrolytes via Kinetic Monte Carlo and Regression Analysis

Ai Koizumi, Mariia Ivonina, Ryo Tamura,* and Tomofumi Tada*

Cite This: J. Phys. Chem. C 2026, 130, 3897−3908
Read Online

ACCESS | Metrics & More | Article Recommendations | Supporting Information

ABSTRACT: The relationship between dopant configuration and ionic current is critical for designing solid-state devices composed of ionic conductors, and this relationship becomes more important when the device is fabricated to a smaller size in device miniaturization. However, this relationship is still ambiguous due to limitations in experimental measurements. In this study, we focused on yttria-stabilized zirconia (YSZ) as a representative ionic conductor and theoretically investigated the relationship between the dopant (yttrium) configuration and ionic current density in 8 mol % YSZ by a data-driven approach. Using a large data set of over 2000 YSZ systems with different yttrium dopant configurations, drift current caused by the oxygen ions diffusing under a bias voltage was calculated using mesoscale kinetic Monte Carlo simulation. To characterize the dopant configurations, three types of physically motivated structural descriptors were defined as histograms of the 6-site local configurations related to oxygen migration and compared with respect to ionic conductivity prediction accuracy. This prediction was conducted using a linear regression model trained on the data set of dopant configurations converted to structural descriptors and calculated ionic conductivities. As a result, we succeeded in identifying the most informative structural descriptors and linking microscopic dopant configurations and macroscopic ionic transport features through multiple computational and data-analytic tools. Furthermore, we found that features related to the waveform of ionic current density, such as local fluctuations and fast Fourier transform (FFT) coefficients, can also be predicted with high accuracy. Thus, our approach allows reconstruction of the ionic current density from the presented structural descriptors. Although YSZ was selected in this study, the present methods can be applied to other ionic conductors in a similar way.

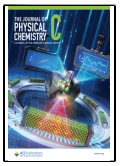


1. INTRODUCTION

The development of first-principles methods has accelerated theoretical research in materials science from an atomistic point of view. The high precision of the first-principles method enables detailed design of electronics, batteries, structural materials, etc., based on energetical stability. In addition, first-principles calculations combined with perturbation techniques and dynamics are also useful to investigate kinetic and dynamical properties by assuming the system is close to the equilibrium state. Therefore, establishing a relationship between the atomistic (i.e., microscopic) structure and macroscopic material properties enables the inverse design of functional materials.[1−3] However, energy-based approaches are not always valid for material design because the fundamental properties of materials in nonequilibrium states are often better described by quantities intrinsic to those conditions. For example, ionic flux (or current) is a key nonequilibrium quantity for energy conversion systems at working conditions, and investigating the relationship between the microscopic structure and current is required for advanced materials design.[4]

Ionic current is an important property in many electrochemical devices, such as energy conversion and gas-sensing devices, and especially, the enhancement of ionic conductivity is directly related to improving device performance. For example, the ionic conductivity in ionic conductors has been investigated as a function of various compositions and dopant concentrations, as well as thin film thickness ranging from the nano- to microscale, and the device performances have been discussed from various perspectives, such as processing techniques used in the epitaxial crystal growth (e.g., pulsed laser deposition (PLD)) and microscopic structures (e.g., changes in lattice parameters and surface densification), measured by X-ray diffraction (XRD) and scanning electron microscopy (SEM).[4−6] However, the relationship between

Received: October 4, 2025
Revised: February 2, 2026
Accepted: February 23, 2026
Published: March 2, 2026



ACS Publications
© 2026 The Authors. Published by American Chemical Society

https://doi.org/10.1021/acs.jpcc.5c06852
J. Phys. Chem. C 2026, 130, 3897−3908

Downloaded from pubs.acs.org/jpccck/article-pdf/130/10/3897/6422852/jp5c06852.pdf by NATL INST FOR MATLS SCIENCE (NIMS) user on 15 September 2026

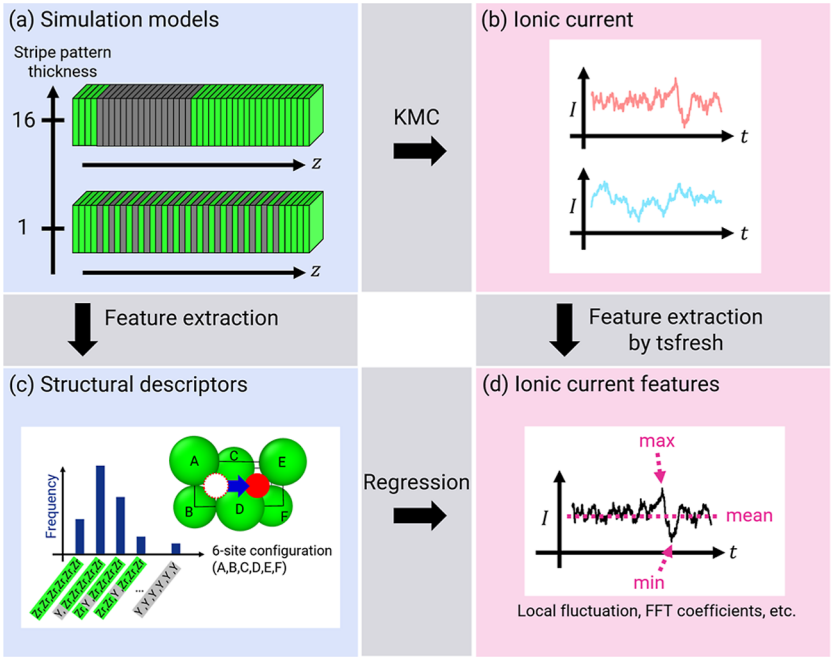


Figure 1. Schematic illustration of the procedure of ionic current feature prediction. (a) The simulation models generated with different stripe pattern thicknesses. (b) The ionic current densities I calculated for all simulation models using kinetic Monte Carlo (KMC) simulation. (c) The histograms of 6-site configurations related to oxygen migration were defined, and the structural descriptors were defined based on these histograms. (d) The ionic current densities I converted to 732 ionic current features using tsfresh. To extract the relationship between the structural descriptors (c) and each ionic current feature (d), the linear regression models with elastic net regularization were trained.

microscopic structure and ionic current is still ambiguous because it is difficult to clarify the micro-to-macro relationship in experiments due to measurement limitations. To realize advanced materials design for solid oxide fuel cells (SOFCs),[4,7−11] understanding the relationship between the microscopic structure and ionic current is necessary. To investigate microscopic phenomena in detail, molecular dynamics (MD) and kinetic Monte Carlo (KMC) simulations are useful techniques. For example, Lee et al. investigated the equilibrium microscopic structures of yttria-stabilized zirconia (YSZ) and gadolinia-doped ceria thin film surface systems. They conducted a hybrid MC−MD algorithm to allow the position exchange of heavy cations, which hardly move in the normal MD simulation, and reported that surface dopant segregation is consistent with the observed results using techniques like X-ray electron spectroscopy (XPS), low-energy ion scattering (LEIS), etc.[12] Madhual and Kumar used MD simulation to investigate the dependence of ionic conductivity based on the Nernst−Einstein relation (i.e., ionic conductivity estimated using diffusion coefficient D), lattice parameter, and energy barrier of oxygen migration on the dopant concentration in the bulk yttria-doped ceria system in the case of random dopant configuration.[13] Tarancón et al. investigated oxygen diffusion by comparing random and layered distributions of dopant yttrium (Y) in yttria-stabilized zirconia (YSZ), which is a representative ionic conductor for the SOFC, using MD simulations. They reported that oxygen ions diffuse isotopically in a system with a random distribution of dopants Y. On the other hand, in a system with layered dopant Y distribution, oxygen ions diffuse along the layer in which the dopants Y are introduced.[14] However, while accurately capturing diffusion processes with small time steps, such MD simulations are computationally expensive and often impractical for studying ionic current, which requires much larger time steps. Thus, it is difficult to investigate the relationship between the dopant configuration and the ionic conductivity using the MD simulation. KMC simulations allow the simulation of ionic conductivity, based on activation barriers predicted by first-principles electronic structure calculations. Hein et al. calculated the mean square displacement of mobile ions in the direction of the electric field using KMC simulations, and they determined ionic conductivities in the bulk system for over 250 materials, where dopant configurations were randomly distributed.[15,16] Furthermore, Tada et al. have developed a parallelized KMC code with the grand canonical framework; this enables the simulation of long-time ion dynamics in large-scale systems (up to the mesoscale) and allows microscopic analysis of nonequilibrium properties such as ionic current with direct counting of passing-through ions under working conditions.[17−19]

In this study, to investigate the relationship between the dopant configuration and the ionic currents, we conducted long-time-scale KMC simulations[17−19] to calculate the ionic current densities under a bias voltage for 2016 systems with different dopant Y configurations (1916 systems with striped pattern distribution of dopants Y and 100 systems with random distribution of dopants Y) in the bulk 8 mol % YSZ (8YSZ) system. Furthermore, we defined structural descriptors related to oxygen migration and analyzed the relationship between the microscopic structure and ionic current density by a data-driven approach. The overview of this study is summarized in Figure 1.

The paper is organized as follows. In Section 2, the method and conditions of the present KMC simulations are explained. The reason to select a stripe pattern, used to generate simulation models with diverse dopant Y configurations, is also explained. In Section 3, three types of structural descriptors are defined to describe microscopic dopant Y configurations, and

https://doi.org/10.1021/acs.jpcc.5c06852
J. Phys. Chem. C 2026, 130, 3897−3908

Downloaded from pubs.acs.org/jpccck/article-pdf/130/10/3897/6422852/jp5c06852.pdf by NATL INST FOR MATLS SCIENCE (NIMS) user on 15 September 2026

732 ionic current features are introduced to characterize ionic current densities. In Section 4, the procedure for the prediction of ionic current features is explained. In Section 5, the results of the prediction of ionic current features are presented and discussed. First, we will focus on the data distribution for all simulation models. The data distributions in the structural descriptor space and in the ionic current feature space will be presented. Next, we will focus on the ionic conductivity as a representative ionic current feature and show the data distribution of all ionic conductivities as a function of a stripe pattern thickness. Then, three types of structural descriptors, defined in this paper, will be discussed and compared with respect to ionic conductivity prediction accuracy. Finally, we will discuss the other ionic current features besides ionic conductivity and show that the local fluctuation and fast Fourier transform (FFT) coefficients of ionic current densities can also be predicted with high accuracy using structural descriptors. The variables and indices used in this paper are summarized in Table S1 in the Supporting Information.

2. METHOD AND CONDITIONS FOR IONIC CURRENT CALCULATIONS

2.1. KMC Method with Applied Bias Voltage

Let us first briefly describe the KMC method for propagating the system's time evolution.[20] In the KMC simulation, it is necessary to obtain a list of all possible events, such as ion hops and chemical reactions. Each event is characterized by its activation barrier E^a, and the reaction probability of the ith event can be represented as $r_i = \nu_i \exp(-\beta E_i^a)$, where ν_i is a pre-exponential factor of the ith event, β is $1/k_BT$, k_B is the Boltzmann constant, and T is the temperature. E_i^a and ν_i can be obtained as temperature-independent parameters from first-principles electronic structure calculations. When the temperature dependence on these parameters is required, the multicanonical free energy sampling approach can be adopted.[19] In this study, the bulk YSZ was selected as a representative ionic conductor for SOFC, for which we defined in advance all 64 possible six-site local configurations that characterize oxygen vacancy migration through two adjacent tetrahedra, as shown in Figure 2. For the bulk YSZ system employed in this study, the migration of oxygen vacancies through the oxygen ions (i.e., a simple exchange of the positions of oxygen vacancy and oxygen ion) is the only event considered in the KMC simulation. The 64 migration energy barriers E_i^a are summarized in Table S2, and ν_i was set to 10^{13} for all migration events. To select a single event among all possible events in a statistical way, we first calculate the sum of all reaction probabilities as $R^{tot} = \sum_i r_i p_i$ and the cumulative sum from the first to jth event as $R_j^{tot} = \sum_{i=1}^{j} r_i p_i$, where p is the binary function taking values of 0 (forbidden) or 1 (allowed) to express whether corresponding events can occur. The binary function p is determined for each oxygen vacancy (index n), each direction (index d), and each 6-site local configuration (index m) as $p_{n,d,m}$. When the migration of the nth oxygen vacancy in the dth direction matching the mth configuration is allowed/forbidden, then $p_{n,d,m} = 1/0$. In the case when there is an oxygen vacancy in the final position of two adjacent tetrahedra, the oxygen vacancy migration is also forbidden and $p_{n,d,m} = 0$. For simplicity, the binary function $p_{n,d,m}$ is represented here as a one-dimensional array p_i. Using random number $\gamma \in [0,1]$, a single event that holds the relationship

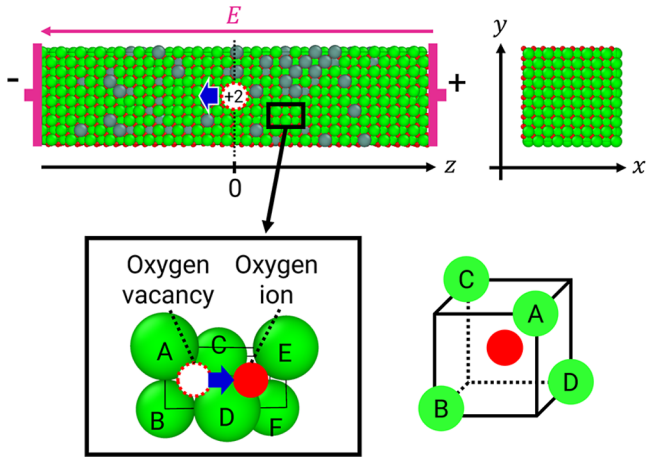


Figure 2. Schematic illustration of the 8YSZ system with the electric field along the z axis. The system is composed of 1680 Zr (green balls), 320 Y (gray balls), and 3840 oxygen ions (red balls) and 160 oxygen vacancies (illustrated as a white circle). Ionic current density was calculated by counting the net number of passing oxygen vacancies through the $x-y$ plane at $z = 0$. Oxygen vacancy migrations occur at the black-framed two adjacent tetrahedra constructed by six Zr/Y (lattice ion) sites. Poisson grids are located at vertices of cubic crystals composed of four lattice ion sites (A–D) and one oxygen ion/vacancy site (mobile ion site).

$\gamma R^{tot} \in [R_{j-1}^{tot}, R_j^{tot}]$ is determined, and the configuration of oxygen vacancies in the system is updated by executing the jth event. The time step of the system is updated by using another random number, $\gamma' \in [0,1]$ as $\Delta t = -\log(\gamma')/R^{tot}$, and p_i is also updated depending on the new configuration of oxygen vacancies.

The effect of the applied bias voltage as the electrostatic energy change ΔE is included into the activation barriers as $E^a + \Delta E$; that is, the reaction probability of the ith event becomes

$$r_i = \nu_i \exp(-\beta(E_i^a + \alpha_b \Delta E_i)) \quad (1)$$

where the balance parameter α_b is selected as 0.5.[21] To calculate ΔE, we adopt the Poisson equation as

$$\nabla(\varepsilon(\boldsymbol{r})\nabla\phi(\boldsymbol{r})) + \rho(\boldsymbol{r}) = 0 \quad (2)$$

where ε, ϕ, ρ, and $\boldsymbol{r}$ are the relative permittivity, electrostatic potential, charge density, and grid position, respectively. For the event between chemical species x_1 and x_2 represented as $x_1(\boldsymbol{r}_1) + x_2(\boldsymbol{r}_2) \rightarrow x_2(\boldsymbol{r}_1) + x_1(\boldsymbol{r}_2)$ (i.e., a simple exchange of the positions), one can calculate electrostatic energies of configurations before the reaction $x_1(\boldsymbol{r}_1) + x_2(\boldsymbol{r}_2)$ and after the reaction $x_2(\boldsymbol{r}_1) + x_1(\boldsymbol{r}_2)$ as $q_{x1}\phi(\boldsymbol{r}_1) + q_{x2}\phi(\boldsymbol{r}_2) \equiv E_{before}$ and $q_{x2}\phi(\boldsymbol{r}_1) + q_{x1}\phi(\boldsymbol{r}_2) \equiv E_{after}$, respectively, where q_x is the charge of species x. Strictly speaking, the electrostatic potentials before and after the reaction should be calculated independently, but we assume that the difference between these electrostatic potentials is negligibly small because the system size in KMC simulations is quite large. Therefore, we adopted an electrostatic potential ϕ before a reaction for the calculations of both E_{before} and E_{after}. Using E_{before} and E_{after} with the approximation, we calculate ΔE for each event as $E_{after} - E_{before}$. For the events happening at the Poisson cell boundaries, we do not include ΔE for the events in order to avoid an artificial effect caused by the so-called sawtooth potential typical for the periodic-with-bias voltage models.

Downloaded from pubs.acs.org/jpccck/article-pdf/130/10/3897/6422852/jp5c06852.pdf by NATL INST FOR MATLS SCIENCE (NIMS) user on 15 September 2026

https://doi.org/10.1021/acs.jpcc.5c06852
J. Phys. Chem. C 2026, 130, 3897−3908

In this study, we calculate ionic current density by directly counting ions passing through a plane[18] perpendicular to the direction of applied bias. In this study, the $x-y$ plane at $z = 0$ in Figure 2 was used for counting passing ions along the z direction. We denote the ionic current density obtained by direct counting as the flux-based current density J^{f}. The raw KMC output of J^{f} demonstrates strong fluctuations, as shown in Figure S1. To suppress the noise and identify long-time trends in time-series data, several averaging techniques can be implemented, such as simple block averaging, simple moving averaging, and exponential moving averaging, which are validated in terms of the relationship between time average and ensemble average, according to the ergodic theorem.[22] In this study, we adopted the following two averaging methods (see Figure S2): the first is simple block average (SBA) as

$$\begin{aligned} J_l^{\mathrm{f_{SBA}}} &\equiv J^{\mathrm{f_{SBA}}}(t_{1+(l-1)N}) \\ &= \frac{1}{N}\sum_{k=1}^{N} J_{k+(l-1)N}^{\mathrm{KMC}},\ l \\ &= 1, 2, 3 ..., \frac{K}{N} \end{aligned} \tag{3}$$

and the second is simple moving average (SMA) as

$$\begin{aligned} J_l^{\mathrm{f_{SMA}}} &\equiv J^{\mathrm{f_{SMA}}}(t_{1+(l-1)N}) \\ &= \frac{1}{N'}\sum_{k'=l}^{l+N'-1} J_{k'}^{\mathrm{f_{SBA}}},\ l \\ &= 1, 2, 3 ..., \frac{K}{N} - (N' - 1) \end{aligned} \tag{4}$$

SBA was applied first to reduce the number of J^{f} output data points, and SMA was used next to further smooth out the fluctuations. J_k^{KMC} is the ionic current density obtained by directly counting ions passing through a certain plane between the (k-1)th and kth KMC steps, and t_k corresponds to the time at the kth KMC step. Parameters N and N' are the number of data points used in SBA and SMA, respectively (i.e., window sizes). If there are K instances of $J_k^{\mathrm{KMC}}(K \gg N)$, then the simple block averaging results in K/N averaged instances of $J^{\mathrm{f_{SBA}}}$, and the simple moving average results in K/N-(N'-1) average instances of $J^{\mathrm{f_{SMA}}}$. We found that the mean value of flux-based current density J^{f} converges quickly with respect to the window sizes for both averaging methods; the details are shown in Figure S1. In this study, window sizes $N = 100$ (for SBA) and $N' = 100$ (for SMA) were adopted for processing the flux-based current density J^{f}.

We also calculated the ionic current density using the diffusion coefficient D of oxygen ions to clarify the difference between the flux-based current density J^{f} and diffusion-based current density J^{d}. J^{d} can be represented through D as

$$J^{\mathrm{d}} = \frac{n_{\mathrm{O}} q_{\mathrm{O}}^2}{k_{\mathrm{B}} T} DV \tag{5}$$

where n_{O} is the number of oxygen ions per cell and q_{O} is the ionic charge of oxygen ions. The temperature T and applied bias voltage V correspond to those used for the calculations of J^{f}.

2.2. Computational Conditions of KMC Simulations

In this section, we explain the computational conditions of the conducted KMC simulations of ionic dynamics in the YSZ system. The YSZ has the cubic zirconia (ZrO_2)-based structure, in which Zr is partly substituted by the dopant Y. O, Zr, and Y ions are formally charged as 2−, 4+, and 3+, respectively, and oxygen vacancies (V_O) are introduced to hold the charge neutrality. Due to oxygen diffusion through the oxygen vacancies, ionic current is expected to appear at a high temperature. Thus, we define Zr/Y as lattice ions and O/V_O as mobile ions in this paper. The ionic conductivity of the YSZ was continuously and widely investigated by many groups as a function of the concentration of yttria (Y_2O_3), and it has been reported that the highest ionic conductivity is achieved when the concentration of yttria is about 8 mol %,[23] which is defined as 8YSZ, so we adopted this dopant concentration in this study. As shown in Figure 2, the unit cell of 8YSZ has a fluorite structure, and the z direction corresponds to the [001] direction. Focusing only on lattice ions (Zr/Y), the models can be characterized as systems of 40 layers of lattice ions in the z direction and 10 layers of lattice ions in both the x and y directions. In this study, we focus on the mean value of ionic current density, $\overline{J^{\mathrm{f_{SMA}}}} = \frac{1}{N}\sum_l^N J_l^{\mathrm{f_{SMA}}}$, where N is here the size of $J^{\mathrm{f_{SMA}}}$, as the most important feature because it is directly related to the ionic conductivity and thus is important for improving device performance. We first investigated the dependence of $\overline{J^{\mathrm{f_{SMA}}}}$ on the system size in the z direction, and we confirmed that the model with 40 layers in the z direction shows sufficient convergence for $\overline{J^{\mathrm{f_{SMA}}}}$ (see Figure S3). We also confirmed $\overline{J^{\mathrm{f_{SMA}}}}$ is almost unchanged even when the model size is increased along the x and y directions (see Figure S4). Thus, the simulation model with the system composed of 40 × 10 × 10 layers of the lattice ions was adopted in this study. The interlayer distance is 2.575 Å, and a layer on the $x-y$ plane has 50 lattice ions. To maintain a constant 8YSZ concentration, 320 out of 2000 Zr sites were substituted by the dopant Y in all simulation models. Thereby, the system is composed of 1680 Zr, 320 Y, and 3840 oxygen ions (O) and 160 oxygen vacancies (V_O). In this study, we investigated the ionic current density while changing only the dopant Y configuration at a constant lattice crystal structure. The initial oxygen vacancy distribution was randomly generated by using a fixed random seed. The periodic boundary condition (PBC) for the ion migrations was adopted in all x, y, and z directions. However, as mentioned in Section 2.1, we applied a bias voltage along the z axis in a stepwise form; we set the electrostatic potential of −0.01 V (+0.01 V) at the left (right) cell boundary to impose an electric field of 0.0002 V/Å across the system. Due to the fixed boundary condition on the electrostatic potentials, charged oxygen vacancies are moderately accumulated to compensate for the fixed potentials at the edges (see Supporting Information Note A).

To solve Poisson eq 2 and take into account the drift force due to the bias voltage, the charges of each element are required. Although the charges of O, Zr, and Y ions in the YSZ are formally assigned as −2, +4, and +3, respectively, it is more suitable in KMC simulations to adopt V_O as a migrating object and use alternative formal charges such as +2 for V_O, 0 for Zr, and −1 for Y. However, since the energy barriers from electronic structure calculations (i.e., E_i^{a} in eq 1) already include the electrostatic effects between charged ions, using formal charges in the Poisson equation to calculate ΔE in eq 1 can result in overestimation of electrostatic energy. To avoid it,

Downloaded from pubs.acs.org/jpccck/article-pdf/130/10/3897/6422852/jp5c06852.pdf by NATL INST FOR MATLS SCIENCE (NIMS) user on 15 September 2026

https://doi.org/10.1021/acs.jpcc.5c06852
J. Phys. Chem. C 2026, 130, 3897−3908

we modified the charges of Zr and Y as −0.16 for both while keeping +2 for V_O, so the counter charges against V_O are homogeneously distributed to lattice ions with the opposite sign, like a background charge. The grid points for solving the Poisson equation were placed at vertices of cubic crystals composed of four lattice sites and one mobile ion site, as shown in Figure 2; thus, the width of the equally spaced Poisson grid elements was 2.575 Å. In eq 2, $\varepsilon(\boldsymbol{r})$ was set to 27 for all Poisson grid elements, corresponding to the experimental bulk 8YSZ system,[24] and T was set to 1050 K as a typical operation temperature for YSZ in SOFC. The electric field was set to 0.0002 V/Å (= 0.02 MV/cm) along the z axis.

Note that in all simulation models, we kept the four layers at both left and right edges along the z direction as pure ZrO_2 layers (i.e., without dopant Y ions) while substituting with dopant Y the 32 layers in the middle area, as shown in Figure 2. It was done to eliminate the effect of oxygen vacancy accumulation at the edges, and more details are given in Supporting Information Note A.

As mentioned in Section 1, our target is investigating ionic current density while changing the dopant Y configuration. Realistically, however, it is impossible to investigate all dopant configurations due to combinatorial explosion. As reported by Tarancón et al., there are clearly differences between the system with random and layer dopant distribution on oxygen diffusion.[14] Thus, we anticipate that the stripe pattern model composed of layered dopant distribution is suitable to extract diverse ionic current density from the bulk 8YSZ, and the obtained relationship is available for crystal design in experiments. In this study, the ionic current density was investigated as a function of the thickness of the Y-rich layers alternating with the ZrO_2 layers in the z direction, forming a stripe pattern, as shown in Figure 1a: in the gray layers (denoted as G), 20 out of 50 Zr sites are randomly substituted by dopant Y (corresponding to 20 mol % YSZ, 20YSZ), and in the light green layers (denoted as L), there is no dopant Y (corresponding to pure ZrO_2). The systems are characterized by the number of directly connected layers of the same color. For example, GLGLGLGL···GL corresponds to the case where the stripe pattern thickness is equal to 1 (Thickness 1), and GGLLGGLL···LL corresponds to the case where the stripe pattern thickness is equal to 2 (Thickness 2). Note that the widths of the adjacent layers in the stripe pattern were kept equal for every thickness. We constructed systems with thickness numbers of 1, 2, 4, 8, and 16, and for these systems, we generated 128, 128, 192, 192, and 1276 simulation models, respectively, with random dopant Y distribution in G layers. Note that all of the simulation models were generated using different random seeds for Y in each G layer and do not contain duplicate structures. We also constructed 100 YSZ bulk systems in which the stripe pattern was omitted and all 32 layers in the middle area were randomly substituted by dopant Y.

Because the migration energy barriers of the moving oxygen vacancies depend on the nearest six sites formed by the lattice ions (green balls A−F in Figure 2) around the migration path, the number of ways to substitute Zr with Y in these 6 sites is 2^6 (= 64). The migration energy barriers E^a were already calculated for 42 out of 64 cases by Pornprasertsuk et al. using density functional theory.[25] The missing cases were estimated in this study by the approach of Grieshammer et al. using the following equation:[26]

$$E^a_{ABCDEF} = E^a_{ZrZrCDZrZr} + (E^a_{ABZrZrEF} - E^a_{ZrZrZrZrZr}) \tag{6}$$

Here, A, B, C, D, E, and F are the indices of 6-site lattice ions (Zr or Y). For three terms on the right side of eq 6, the migration energy barriers E^a, calculated by Pornprasertsuk et al., were used. All migration energy barriers E^a are summarized in Table S2. The estimation accuracy was discussed using 24 cases of known migration barriers in Supporting Information Note B. In addition, we investigated the sensitivity of the precision of the estimated barriers on ionic conductivity/local fluctuation of currents, and we concluded that these current features are not significantly affected by the precision of the migration barrier estimation at a temperature of 1050 K (See Supporting Information Note C). The KMC simulations were conducted to obtain 2 μs of ionic current densities j^{SMA}, where the first 1 μs was excluded for the equilibration, and the data output of the remaining time was analyzed; we confirmed the oxygen vacancy distribution is sufficiently equilibrated after 1 μs (see Supporting Information Note D). All of the KMC conditions are summarized in Table S3.

3. DESCRIPTORS

3.1. Microscopic Structural Descriptors

In this section, three types of structural descriptors will be defined. All descriptors are constructed based on histograms showing the frequency distribution of the present 6-site local configurations forming the oxygen vacancy migration path in the six directions, as $+x$, $-x$, $+y$, $-y$, $+z$, and $-z$ directions, as shown in Figure 1c. The histogram is formed by 64 bars, each corresponding to a six-site local configuration (adjacent tetrahedra of lattice ions) from Table S2, via counting how many of these configurations appear in the systems along the x, y, and z directions separately. For example, the value of the histogram bar h of the local configuration m in the case when the mobile ion sites migrate in the $+z$ direction is calculated as follows:

$$h^{+z}_m = \sum_{n'=1}^{N_M} P^{+z}_{n',m} \tag{7}$$

where N_M is the number of all mobile ion sites in the system and $P_{n',m}$ is a binary function (i.e., 0: absent, 1: present). Here, $P^{+z}_{n',m}$ is defined for the migrations in the $+z$ direction for each mobile ion site (index n') for each 6-site local configuration (index m). Note that the binary function $P_{n',m}$ is determined once dopant Y positions are assigned in the model and does not depend on the oxygen occupation at the mobile ion sites, unlike the binary function p_i in Section 2.1. For example, for the migration in the $+z$ direction inside the n'th mobile ion site (A,B,C,D,E,F) = (Zr, Zr, Zr, Zr, Zr, Zr) with the index m = 1, $P^{+z}_{n',1} = 1$, and all the remaining 63 values of $P^{+z}_{n',m\neq 1}$ for this n'th site are equal to 0. Thus, the total number of the accounted mobile ion sites in the system is conserved, according to the following equations:

$$\sum_{m=1}^{64} P^{+z}_{n',m} = 1, \ \forall\ n' \tag{8}$$

$$\sum_{m=1}^{64} h^{+z}_m = N_M \tag{9}$$

https://doi.org/10.1021/acs.jpcc.5c06852
J. Phys. Chem. C 2026, 130, 3897−3908

Downloaded from pubs.acs.org/jpcccck/article-pdf/130/10/3897/6422852/jp5c06852.pdf by NATL INST FOR MATLS SCIENCE (NIMS) user on 15 September 2026

In the same way, h_m^{-z}, h_m^{+x}, h_m^{-x}, h_m^{+y}, and h_m^{-y} are defined for migrations in the $-z$, $+x$, $-x$, $+y$, and $-y$ directions, respectively. Therefore, when the configuration of dopant Y in the system is determined, these histograms are explicitly determined too. In addition, these histograms can be calculated for each layer along the z direction. In this case, the value of the histogram bar corresponding to the layer in a certain z position is obtained as follows:

$$h_m^{+z}(z) = \sum_{n'=1}^{N_M(z)} P_{n',m}^{+z}(z) \tag{10}$$

where $N_M(z)$ represents the number of mobile ion sites in the zth layer. Similarly, the total number of the accounted mobile ion sites in all layers in the system is conserved, according to the following equations:

$$\sum_{m=1}^{64} P_{n',m}^{+z}(z) = 1, \forall\, n' \tag{11}$$

$$\sum_{z=1}^{N_{layer}} \sum_{m=1}^{64} h_m^{+z}(z) = N_M \tag{12}$$

where the number of layers along the z direction N_{layer} is equal to 40 in this study.

Due to the drift forces acting on the oxygen vacancies under the applied weak bias voltage, the ionic current is weakly forced to flow in the z direction. Therefore, we expect that the structural descriptors along the z direction (i.e., h_m^{+z}, h_m^{-z}) are important. However, the importance of the descriptors along the x and y directions and the effect of dividing the histograms by layers in the z direction might also be valuable. Thus, we considered the three following types of structural descriptors:

$$\boldsymbol{d}_{zxy}^{bulk} = (\{h_m^{+z}, h_m^{-z}, h_m^{xy}\}_{m=1,\ldots,64})$$

$$\boldsymbol{d}_{z}^{layer} = (\{h_m^{+z}(z), h_m^{-z}(z)\}_{m=1,\ldots,64,z=1,\ldots,N_{layer}})$$

$$\boldsymbol{d}_{zxy}^{layer} = (\{h_m^{+z}(z), h_m^{-z}(z), h_m^{xy}(z)\}_{m=1,\ldots,64,z=1,\ldots,N_{layer}})$$

where h_m^{xy} is defined as follows:

$$h_m^{xy} = \sqrt{(h_m^{+x} - h_m^{-x})^2 + (h_m^{+y} - h_m^{-y})^2} \tag{13}$$

These combined descriptors are defined by one-dimensional vectors with the corresponding dimensions M of 192 (64 × 3), 5120 (64 × 40 × 2), and 7680 (64 × 40 × 3). All simulation models (N_d = 2016) were transformed into these structural descriptors, resulting in three $N_d \times M$ matrices. Features with very small variance were excluded using the variance threshold approach.[27] In practice, features with a variance of less than 10^{-10} were removed.

3.2. Ionic Current Features

The time series data of the ionic current density, $J^{f_{SMA}}$, were calculated in the KMC simulations. However, since the length of time steps (Δt) in KMC simulations is not constant and depends on the total sum of reaction probabilities, executing simulations with up to 2 μs may result in different total steps in the $J^{f_{SMA}}$ time series for different models. To remove this KMC-specific character from the time series data $J^{f_{SMA}}$ and align it in a common time frame, the modified ionic current density I was calculated for every simulation model from the $J^{f_{SMA}}$ by an additional SBA procedure with the constant time step Δt_c = 0.002 μs as follows:

$$I_{l'} = \underset{(l'-1)\Delta t_c \le t_l^{SMA} < l'\Delta t_c}{\text{mean}} J_l^{f_{SMA}} \tag{14}$$

where $\underset{(l'-1)\Delta t_c \le t_l^{SMA} < l'\Delta t_c}{\text{mean}}$ is the averaging operation for the data points existing in the range $(l' - 1)\,\Delta t_c \le t_l^{SMA} < l'\,\Delta t_c$ and t_l^{SMA} corresponds to the time of $J_l^{f_{SMA}}$. The resulting ionic current density I was systematically calculated as a function of the stripe pattern thickness, as shown in Figure 1b. Note that this modification causes almost no change from the $J^{f_{SMA}}$ time series. For ionic current feature extraction, tsfresh[28] was used. It defines 783-dimensional time-series features. Among these, 732 features were retained in our data set after removing those with a variance below 10^{-10} using the variance threshold.

4. IONIC CURRENT FEATURE PREDICTION

Using three types of structural descriptors (i.e., $\boldsymbol{d}_{zxy}^{bulk}$, $\boldsymbol{d}_{z}^{layer}$, and $\boldsymbol{d}_{zxy}^{layer}$) defined in Section 3.1, each of the ionic current features was predicted using a regression model with an elastic net regularization, which allows both feature selection and the handling of multicollinearity for structural descriptors. To evaluate the prediction performance, we used the coefficient of determination (R^2) on all test data (all 1916 stripe pattern models) under the leave-one-out cross validation. Linear regression fitting was conducted using the scikit-learn[29] package. In scikit-learn, the strength of regularization is controlled by the hyperparameter α. As α increases, the regularization effect becomes stronger and more structural features are removed. We tested the prediction performance for α = 0.1, 0.001, 0.00001, and 0, and the model with the highest R^2 value was adopted. The dimensions of the structural descriptors are summarized in Tables S4 and S5.

5. RESULTS AND DISCUSSION

5.1. Data Distribution

The data distributions of three types of structural descriptors and ionic current features for all simulation models (N_d = 2016) are shown in Figure 3. Using principal component analysis (PCA) implemented in the scikit-learn package,[29] the data is mapped to the two-dimensional space. Note that a large number of components are required to represent the date distribution shown in Figure 3, indicating the difficulty of providing a simple physical explanation for the resultant axes in PCA. The data distributions depending on the thickness of the stripe patterns are indicated by differences in point colors. We found that all the simulation models based on stripe pattern thickness or random distribution were clustered well and could be clearly distinguished in the two-dimensional space using any of the three types of structural descriptors. In addition, the descriptors that include layer information provide clearer distinction compared to bulk descriptors. In the ionic current feature space, data distribution also depends on the stripe pattern thickness. Thus, the stripe pattern models exhibit diverse dopant Y configurations and ionic current densities. In addition, we found that the data spread of ionic current features increases as the thickness of the stripe pattern increases in Figure 3d; the data distribution of each data set is shown in Figure S5. We suggest two reasons for this behavior. First, we think that this is because several types of migrations cannot happen in the z direction when the stripe

Downloaded from pubs.acs.org/jpccck/article-pdf/130/10/3897/6422852/jp5c06852.pdf by NATL INST FOR MATLS SCIENCE (NIMS) user on 15 September 2026

https://doi.org/10.1021/acs.jpcc.5c06852
J. Phys. Chem. C 2026, 130, 3897−3908

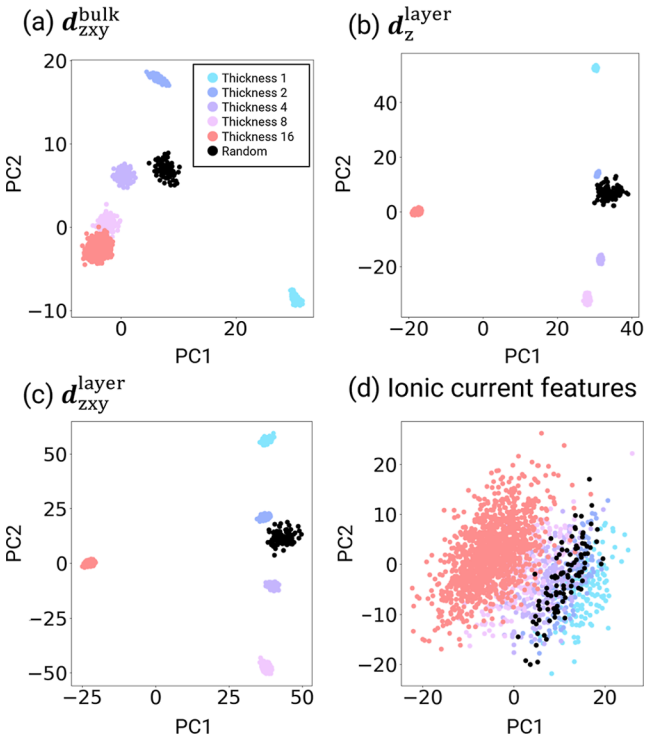


Figure 3. Scatter plots showing data distribution for all simulation models in the two-dimensional space obtained by PCA analysis, corresponding to (a) structural descriptor of d_{zxy}^{bulk}, (b) d_{z}^{layer}, (c) d_{zxy}^{layer}, and (d) ionic current features.

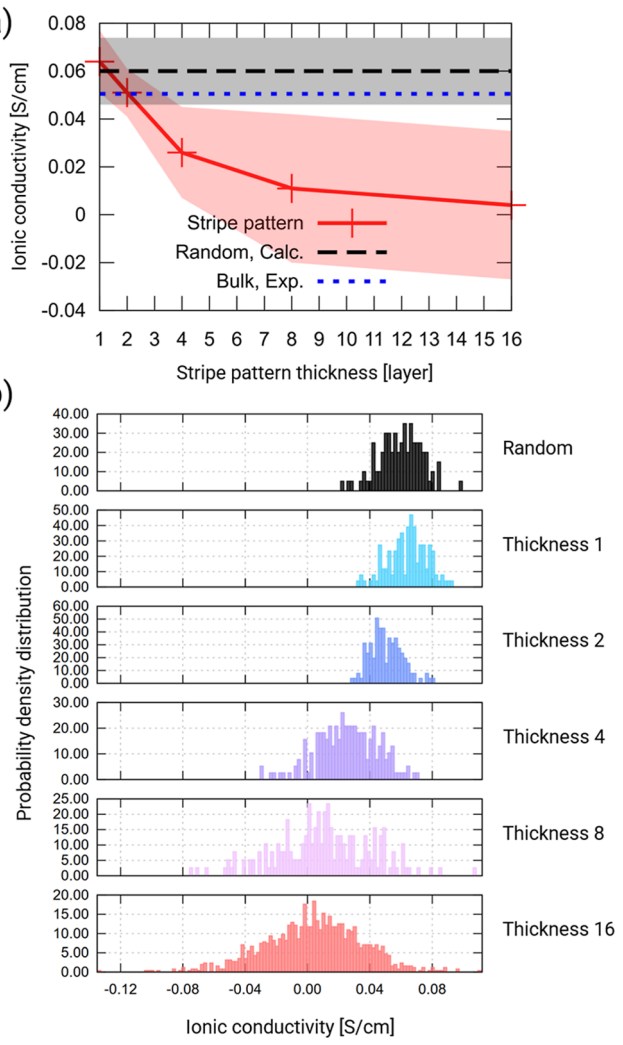


Figure 4. (a) Ionic conductivity as a function of the stripe pattern thickness. The random distribution case and experimental results are also shown. The average value and standard deviation are plotted as lines and shaded areas, respectively. (b) Probability density distributions of the ionic conductivity for each stripe pattern thickness.

pattern thickness is small. In the case where the thickness is 1, the unavailable 6-site local configurations in the z direction are shaded in Table S2. On the other hand, all the 6-site local configurations can exist in the z direction in the case of thickness larger than 2. Second, Y ions are randomly distributed in each Y-rich layer, and the combinations of many directly connected Y-rich layers with different Y configurations produce more diverse 6-site local configurations when the stripe pattern thickness is large. Thus, the diversity of data is increased as the thickness increases.

5.2. Ionic Conductivity Results

In this study, we focus on the mean value of ionic current density, $\overline{I} = \frac{1}{N}\sum_{l'}^{N} I_{l'}(=\overline{J^{f_{SMA}}})$, where N is the size of I, as the most important feature because it is directly related to the ionic conductivity and thus is important for improving device performance. To connect the KMC simulation results to an experimentally measurable quantity, $\overline{I}$ was converted to ionic conductivity by dividing by the applied bias voltage, enabling a comparison with experimental values. Thus, in the rest of this paper, we utilize the ionic conductivity as an equivalent to the mean ionic current density, $\overline{I}$, of each simulation model.

We describe the relationship between the stripe pattern thickness and ionic conductivity that is depicted in Figure 4a. The solid red line represents the average ionic conductivity of all stripe pattern models at each thickness, with the pink shaded area indicating the corresponding standard deviations. For comparison, the average ionic conductivity of models with random dopant substitution and the experimental ionic conductivity of 8YSZ[30] are also shown. Since random substitution can roughly reproduce the actual bulk structure of 8YSZ, it is notable that the experimental ionic conductivity of 8YSZ[30] falls within the standard deviation range of the randomly substituted models. All ionic conductivity results are summarized in Table S6.

The ionic conductivities when the stripe pattern thickness is 1 are the closest to those calculated in the case of random substitution, and the average ionic conductivity decreases as the stripe pattern thickness increases. This tendency is almost converged when the stripe pattern thickness is 16. We think this tendency is reasonable because the migration barriers tend to be high when the number of dopants Y in the 6-site local configurations is high (see Table S2), which is characteristic of models with the larger thickness number. The decreased average conductivity of Thickness 16 roughly corresponds to Lee's calculations on 8YSZ using several patterns of Y distributions, where it is reported that a presence of a highly concentrated Y region results in the decrease of conductivity in comparison with that of random Y distribution.[31] On the other hand, we also found that a specific Y configuration of Thickness 16 results in the maximum conductivity among all the samples investigated in the present study. The reason why

Downloaded from pubs.acs.org/jpccck/article-pdf/130/10/3897/6422852/jp5c06852.pdf by NATL INST FOR MATLS SCIENCE (NIMS) user on 15 September 2026

https://doi.org/10.1021/acs.jpcc.5c06852
J. Phys. Chem. C 2026, 130, 3897−3908

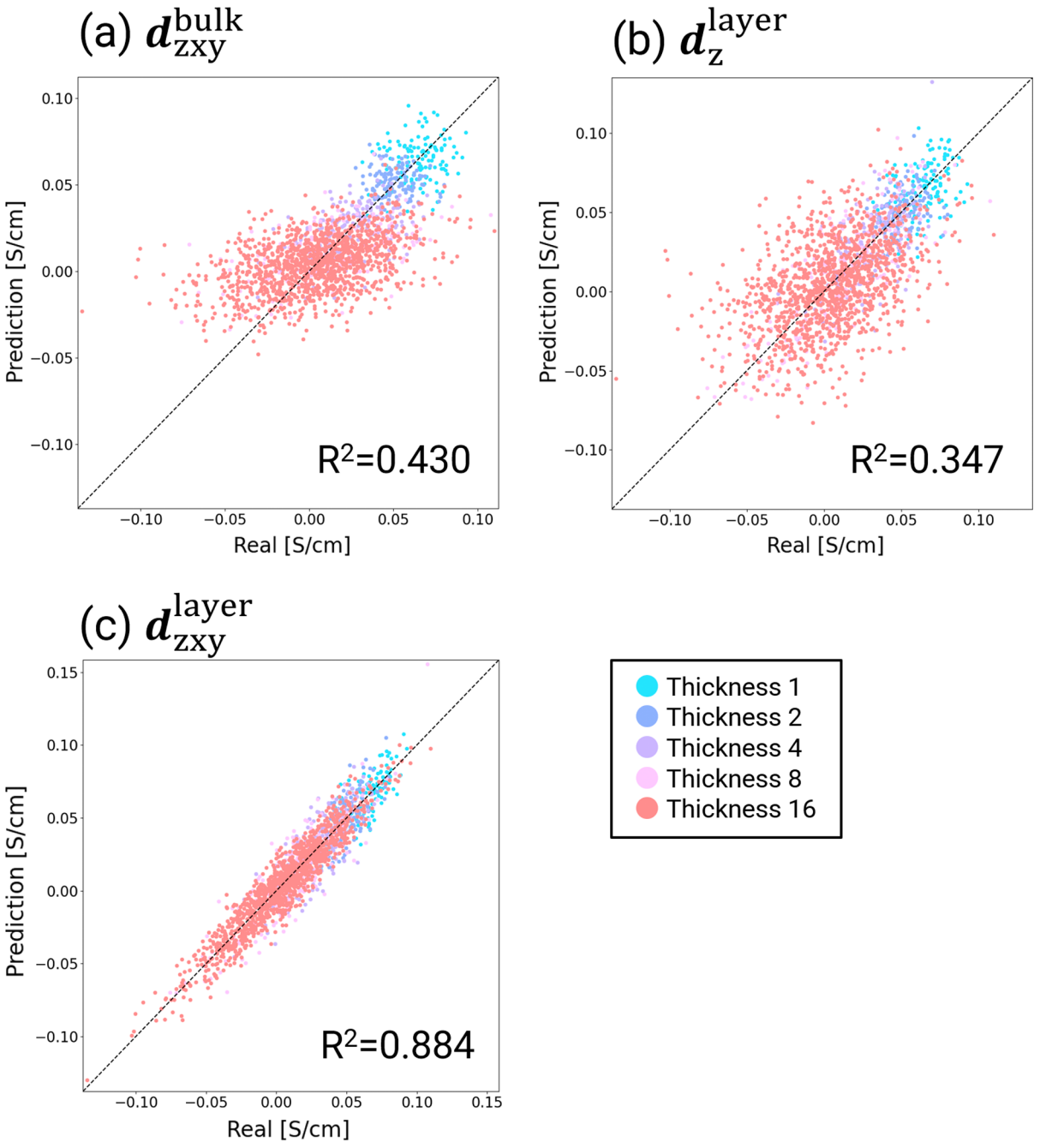


Figure 5. Scatter plots showing the prediction accuracy of ionic conductivities by linear regression with elastic net regularization. Data on panels (a), (b), and (c) are prediction results by using d_{zxy}^{bulk}, d_{z}^{layer}, and d_{zxy}^{layer}, respectively. The horizontal axis is the ionic conductivity calculated using the KMC simulations, and the vertical axis is the predicted ionic conductivity. The difference of thickness is expressed by the different colors.

such a specific Y configuration in Thickness 16 can lead to the enhancement of conductivity will be clarified in a future work.

On the other hand, the variance of the ionic conductivity values increases as the stripe pattern thickness increases. This tendency is similar to the spread of ionic current features shown in Figure 3d. Although the average ionic conductivity decreases as the stripe pattern thickness increases, the highest ionic conductivity was obtained when the stripe pattern thickness is 16, as shown in Figure 4b. This is due to the same reasons described in Section 5.1, i.e., many connected layers with random Y distribution produce diverse 6-site local configurations with different migration barriers, resulting in diverse ionic conductivities.

We also found that the ionic conductivities of many systems are negative when the stripe pattern thickness is large. Negative ionic conductivity means the backward flow of ionic current (the oxygen vacancies flow in the opposite direction in Figure 2) with respect to the direction of the applied bias voltage in the KMC simulations. Generally, the direction of oxygen migration depends on the migration energy barriers E^a, inherent to a certain Y configuration, and the effect of the applied bias voltage ΔE. In this study, the applied bias voltage is quite weak; therefore, the hopping probabilities of oxygen vacancy migrations are mostly dependent on the Y configurations. As a result, there are both cases of Y configurations where vacancies flow more easily in the forward

https://doi.org/10.1021/acs.jpcc.5c06852
J. Phys. Chem. C 2026, 130, 3897−3908

Downloaded from pubs.acs.org/jpccck/article-pdf/130/10/3897/6422529/jp5c06852.pdf by NATL INST FOR MATLS SCIENCE (NIMS) user on 15 September 2026

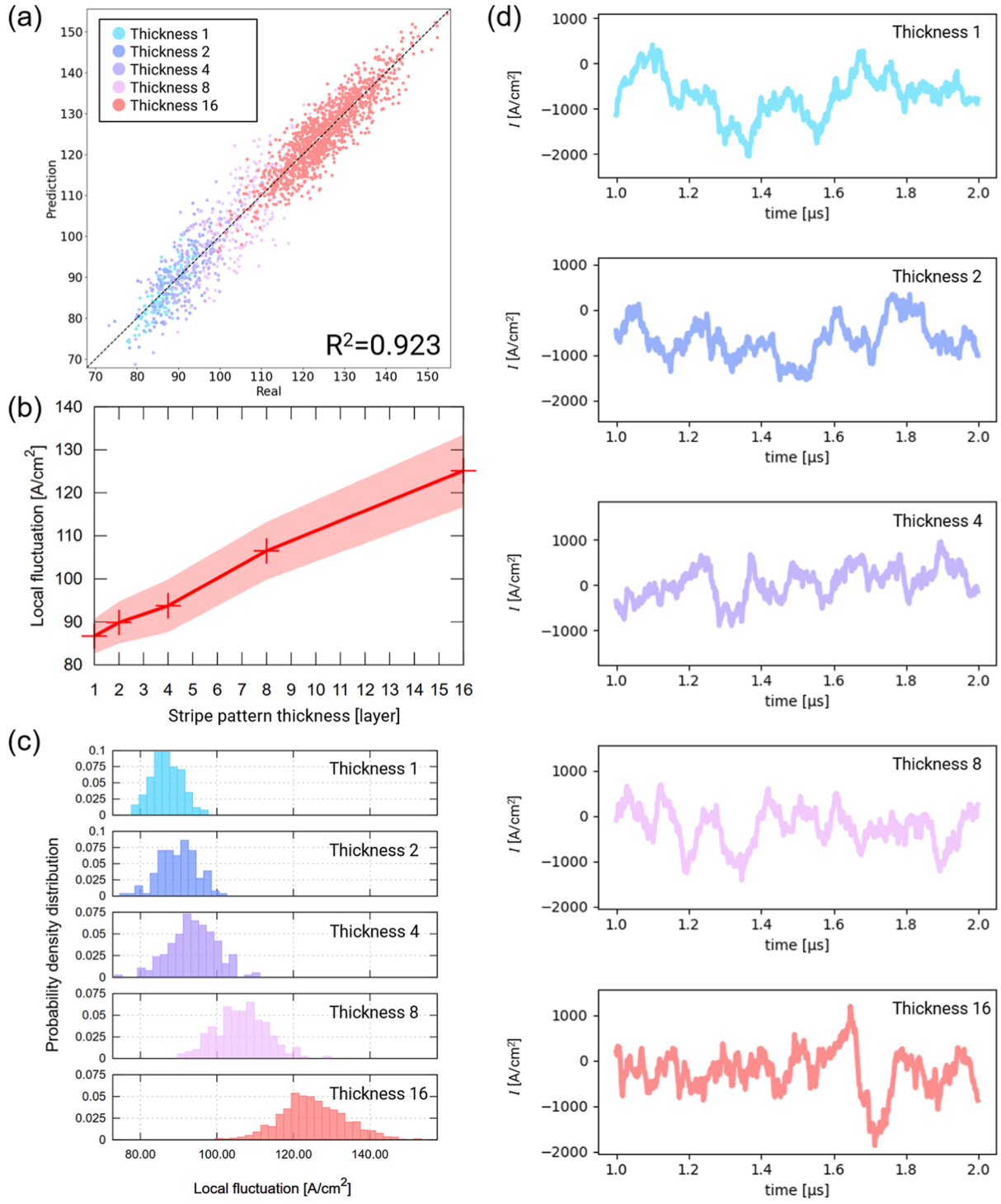


Figure 6. (a) Scatter plot showing the prediction of local fluctuation of ionic current density given in A/cm^2, F_L, conducted using $\boldsymbol{d}_{zxy}^{layer}$. (b) F_L as a function of the stripe pattern thickness. The average value and standard deviation are plotted as a line and shaded area, respectively. (c) Probability density distribution of F_L for each stripe pattern thickness. (d) Calculated ionic currents I for each stripe pattern thickness, whose F_L show closest values to the average value of F_L.

direction and in the backward direction; we discuss the effect of the applied bias voltage on the flux-based ionic conductivity in Supporting Information Note E in detail. As mentioned in Section 2.1, we compare flux-based current density with diffusion-based current density. When the ionic conductivity is estimated using the diffusion-based current density J^d, forward and backward flow cannot be distinguished (see Figure S6). We discussed the difference between the flux-based and diffusion-based ionic conductivity in Supporting Information Note F in detail.

5.3. Ionic Conductivity Prediction

We conducted the ionic conductivity prediction by structural descriptors for the 1916 stripe pattern models using the linear regression model, according to the procedure described in Section 4. The prediction accuracies were compared for the

https://doi.org/10.1021/acs.jpcc.5c06852
J. Phys. Chem. C 2026, 130, 3897−3908

Downloaded from pubs.acs.org/jpccck/article-pdf/130/10/3897/6422852/jp5c06852.pdf by NATL INST FOR MATLS SCIENCE (NIMS) user on 15 September 2026

linear regression models trained using three types of structural descriptors. The results of the ionic conductivity predictions based on the leave-one-out cross validation are shown in Figure 5a−c, where the horizontal axis is the ionic conductivity obtained in the KMC simulations and the vertical axis is the predicted ionic conductivity. The provided plots correspond to the linear regression fits that achieved the highest R^2 values: 0.430 for $\boldsymbol{d}_{zxy}^{\mathrm{bulk}}$ (α = 0.001), 0.347 for $\boldsymbol{d}_{z}^{\mathrm{layer}}$ (α = 0.001), and 0.884 for $\boldsymbol{d}_{zxy}^{\mathrm{layer}}$ (α = 0.00001). Prediction accuracies depending on α are summarized in Table S4. The highest R^2 value when using $\boldsymbol{d}_{zxy}^{\mathrm{layer}}$ indicates that information about the dopant Y configuration in all x, y, and z directions as well as specifying this information in each layer in the z direction is important for predicting ionic conductivity with high accuracy. In addition, we found that the ionic conductivity cannot be accurately predicted when using $\boldsymbol{d}_{z}^{\mathrm{layer}}$ and $\boldsymbol{d}_{zxy}^{\mathrm{layer}}$ descriptors without feature selection (α = 0) as shown in Table S4. This result indicates that the correct choice of the regularization term α is important for $\boldsymbol{d}_{z}^{\mathrm{layer}}$ and $\boldsymbol{d}_{zxy}^{\mathrm{layer}}$. We think there are two reasons for such a behavior. First, the dimensions of the descriptors are larger than the training data size. Thus, feature selection based on regularization is needed to reduce the dimensions of the structural descriptors. Second, all combined structural descriptors have internal multicollinearity. In other words, some explanatory variables are highly correlated. For example, the multicollinearity happens in the case of $h^{+z}(z)$ and $h^{-z}(z)$ histograms, included in $\boldsymbol{d}_{z}^{\mathrm{layer}}$ and $\boldsymbol{d}_{zxy}^{\mathrm{layer}}$. For all layers along the z direction (index z), when there are "Y Y Zr Zr Y Y" configurations in the zth and $(z + 2)$th layers in the $+z$ or $-z$ directions, "Zr Zr Y Y Zr Zr" configurations exist in the same direction in the $(z + 1)$th layer. In this way, the frequency of "Zr Zr Y Y Zr Zr" in the $(z + 1)$th layer and the frequencies of "Y Y Zr Zr Y Y" in the zth and $(z + 2)$th layers are the same in the $h^{+z}(z)$ and $h^{-z}(z)$. Although this multicollinearity occurs frequently in our stripe pattern models, especially when the stripe pattern thickness is 1, we think that it can also occur in other models with various dopant distributions. In elastic net regularization, the term addressing multicollinearity is included, and tuning α is essential for achieving better prediction in our system. In addition, we investigated elastic net regression coefficients using the data set of Thickness 16, and we obtained no clear trend (see Supporting Information Note G). Further investigation will be needed to understand the physics behind the relationship between the microscopic structure and the ionic conductivity.

Here, we discuss the conditions of the KMC simulation. In this study, we adopted the relative permittivity of the bulk 8YSZ, and we used it for all of the Poisson grids, assuming that the simulation models are close to the situation of the bulk 8YSZ system. This assumption seems reasonable in the case of random substitution. However, we investigated the ionic current density changing dopant Y configurations considering the stripe pattern model. Thus, there are a connected 20YSZ layer region, a connected ZrO_2 layer region, and the interface of two regions in many simulation models, and we think these regions are close to the bulk 20YSZ, bulk ZrO_2 systems, and the 20YSZ/ZrO_2 interface, respectively. In such a case, we think that the relative permittivity should also be considered as a function of the dopant configuration in the local environment in eq 2 for further calculation accuracy. However, in this study, the weak bias voltage was adopted to calculate drift ionic current density, and the resultant ΔE value in eq 1 was small in this study. Thus, the reaction probability of oxygen vacancy migration mainly depends on the term E^{a}. Thus, we believe that the effect of adopting a constant relative permittivity for all Poisson grids is small. In addition, the model of the migration energy barrier with the 6-site local configuration was used, and it also seems reasonable to calculate ionic conductivity in the 8YSZ bulk system. However, the migration energy barriers E^{a} used in this study do not consider the situation where the dopant Y condensed system such as the Thickness 16. Thus, to address other systems, i.e., the surface and interface of the SOFC, and to achieve further calculation accuracy, we think that the relative permittivity depending on the local environment should be considered, and the 6-site migration model should also be extended to a broader range model. Although the present results seem reasonable, we believe that further consideration will be required in the future. Please see Supporting Information Notes B and C for the discussion on the estimated migration barriers E^{a} for 22 types of migrations by using eq 6.

5.4. Other Ionic Current Features

In Section 5.3, we succeeded in an accurate prediction of the ionic conductivity using the structural descriptors of $\boldsymbol{d}_{zxy}^{\mathrm{layer}}$. In this section, we focus on other ionic current features. As mentioned above, each ionic current feature has a variance. Thus, we also investigated whether other ionic current features can be predicted by the $\boldsymbol{d}_{zxy}^{\mathrm{layer}}$. The prediction accuracies were investigated for each ionic current feature by fitting the linear regression with elastic net regularization when α is fixed as 0.00001. The ionic current features, predicted with the top 50 highest accuracies, were ranked according to the R^2 values and are listed in Table S7. We found that the local fluctuation (F_{L}) of the ionic current density, denoted as "mean_abs_change" in Table S7, can be accurately predicted with $\bar{R}^2$ = 0.923 (see Figure 6a). The local fluctuation is defined as follows:

$$F_{\mathrm{L}} = \frac{1}{N_{\mathrm{I}} - 1} \sum_{l'=1}^{N_{\mathrm{I}}-1} |I_{l'+1} - I_{l'}| \tag{15}$$

where N_{I} is the size of ionic current density data I, defined as eq 14, and $I_{l'}$ is the value of ionic current density at $l'\Delta t_c$ μs. F_{L} as a function of the stripe pattern thickness is represented in Figure 6b. The average fluctuation and its standard deviation for each stripe pattern thickness are plotted as a line and shaded area, respectively. Figure 6c shows a probability density distribution of F_{L} for each stripe pattern thickness. These results indicate that the local fluctuation of ionic current density increases with an increase of thickness. In Figure 6d, we plot an example of ionic current density time series for each stripe pattern thickness using models with F_{L} close to the mean F_{L} for the corresponding thickness. When the stripe pattern thickness is 16, there is clearly a sharp transition around 1.7 μs in the ionic current density. The ionic current density increases before the transition, which indicates backflow of the ionic current. After that, the ionic current density decreases quickly (i.e., sharp transition), indicating a forward flow. The transitions can also be seen in plots for smaller thicknesses, but for them, the amplitude is moderate.

Although we showed here an example for predicting the local fluctuation of ionic current density, we were able to successfully predict other features related to the shape of the ionic current density in our models, such as the FFT coefficients of multiple frequencies (see Table S7). Since the waveform can be constructed using the FFT coefficients, we believe that the waveform can also be predicted by using the

Downloaded from pubs.acs.org/jpccck/article-pdf/130/10/3897/6422852/jp5c06852.pdf by NATL INST FOR MATLS SCIENCE (NIMS) user on 15 September 2026

https://doi.org/10.1021/acs.jpcc.5c06852
J. Phys. Chem. C 2026, 130, 3897−3908

structural descriptors. Although the present ionic current measurement cannot observe such detailed waveforms, further development of measurement techniques will enable one to obtain the waveform features; we hope that waveform features will be useful for anomaly detection of devices in working condition. Thus, we believe that our approach can be useful for predicting (or reconstructing) the waveform of any ionic conductors through the combinations of predicted ionic current features. This research direction is a part of our future studies of the relationship between microscopic structure and macroscopic properties of ionic conductors.

6. CONCLUSION

In this study, a large data set of over 2000 Y-dopant configurations and ionic currents was obtained by applying the mesoscale kinetic Monte Carlo (KMC) framework. Among the configurations, 100 models were generated by randomly substituting bulk ZrO_2 with dopant Y with no restrictions, while the remaining 1916 models were generated as systems with regular Y-containing layers along the z direction arranged in a stripe pattern with 1, 2, 4, 8, and 16 thicknesses of layers. When substituting YSZ randomly, it is highly probable to find dopant Y in every layer, which leads to a limited range of resulting ionic conductivities and consistent values of experimental conductivity. On the other hand, the stripe pattern models exhibit diverse ionic conductivities, and average conductivity decreases as the stripe pattern thickness increases, while the variance becomes larger. This indicates that the layered dopant distribution can yield conductivities much higher or lower than those expected from random substitution. Although it is not possible to control the detailed dopant arrangements in the experiment, we expect that the stripe pattern of doping can be possible by using epitaxial growth methods such as pulsed laser deposition (PLD) or atomic layer deposition (ALD).

To better capture the relationship between microscopic structures and ionic conductivities, we introduced three structural descriptors based on the histograms of 6-site local configurations relevant to oxygen migrations: (i) information on the dopant Y configuration in the bulk structure in the $+z$, $-z$, and xy directions, (ii) information on the dopant Y configuration in each layer in the $+z$ and $-z$ directions, and (iii) information on the dopant Y configuration in each layer in the $+z$, $-z$, and xy directions. We investigated whether the ionic conductivities of stripe pattern models can be predicted using the linear regression model with elastic net regularization trained on the relationship between the structural descriptors and ionic conductivities. We found that the third descriptor results in the highest prediction accuracy. This highlights the importance of including information about the layer-resolved dopant configurations in both the xy plane and the z direction, even though the ionic current flows primarily along the z direction. This study thus successfully achieved its aim of linking microscopic structure to ionic current in mesoscale kinetic Monte Carlo simulations.

Furthermore, using tsfresh, we applied time-series feature extraction to the 1916 ionic current density data set, resulting in 732 ionic current features. We found that key features such as local fluctuations and FFT coefficients can also be predicted from the structural descriptor with a high accuracy. Thus, we postulate that the ionic current density can be reconstructed using predicted ionic current features from our introduced microscopic structural descriptors.

The combination of large-scale simulations with comprehensive structural sampling represents a significant step toward systematic structure−property mapping in solid electrolytes. Although this study focused on bulk YSZ as a representative ionic conductor for SOFCs, the structural descriptors and techniques introduced here can be extended to other ionic conductors and will be applied to surface/interface systems. We anticipate that the results achieved in this study will contribute to data-driven materials design.

■ ASSOCIATED CONTENT

Supporting Information

The Supporting Information is available free of charge at https://pubs.acs.org/doi/10.1021/acs.jpcc.5c06852.

List of variables and indices; oxygen migration energy barriers; KMC conditions; prediction accuracy with different α; number of dimensions of structural descriptors; ionic conductivity as a function of a stripe pattern thickness; top 50 prediction accuracy ranking for all current features; effect of two types of moving averaging on current density; schematic illustration explaining two types of moving averaging; cell size dependence of ionic conductivity (in the z direction); cell size dependence of the mean value of ionic current (in the x/y directions); data distribution of ionic current features; comparison of flux-based and diffusion-based conductivities; vacancy accumulation; estimation accuracy of migration energy barriers; sensitivity analysis of the estimated migration barrier on ionic conductivity; convergence check for the oxygen vacancy distribution; effect of the applied bias voltage on ionic conductivity; and regression coefficient analysis (PDF)

■ AUTHOR INFORMATION

Corresponding Authors

Ryo Tamura − *Center for Basic Research on Materials, National Institute for Materials Science, Ibaraki 305-0044, Japan; Graduate School of Frontier Sciences, The University of Tokyo, Kashiwa, Chiba 277-8561, Japan;* orcid.org/0000-0002-0349-358X; Email: tamura.ryo@nims.go.jp

Tomofumi Tada − *Kyushu University Platform of Inter/Transdisciplinary Energy Research, Kyushu University, Fukuoka 819-0395, Japan;* orcid.org/0000-0003-3093-3779; Email: tada.tomofumi.054@m.kyushu-u.ac.jp

Authors

Ai Koizumi − *Center for Basic Research on Materials, National Institute for Materials Science, Ibaraki 305-0044, Japan*

Mariia Ivonina − *Kyushu University Platform of Inter/Transdisciplinary Energy Research, Kyushu University, Fukuoka 819-0395, Japan*

Complete contact information is available at: https://pubs.acs.org/10.1021/acs.jpcc.5c06852

Notes

The authors declare no competing financial interest.

■ ACKNOWLEDGMENTS

This study was supported by research grants subsidized by the Core Research for Evolutional Science and Technology (JST

Downloaded from pubs.acs.org/jpccck/article-pdf/130/10/3897/6422852/jp5c06852.pdf by NATL INST FOR MATLS SCIENCE (NIMS) user on 15 September 2026

CREST) (JPMJCR2234) and KAKENHI (J21H01008, 24K21808, 24H02203). The computations in the present study were conducted on the supercomputer at the National Institute for Materials Science. The authors would like to thank Prof. Takashi Washio and Prof. Tomoyuki Higuchi for valuable discussions and insightful comments.

REFERENCES

(1) Zunger, A. Inverse Design in Search of Materials with Target Functionalities. *Nat. Rev. Chem.* **2018**, *2* (4), 0121.
(2) Fung, V.; Zhang, J.; Hu, G.; Ganesh, P.; Sumpter, B. G. Inverse Design of Two-Dimensional Materials with Invertible Neural Networks. *npj Comput. Mater.* **2021**, *7* (1), 200.
(3) Wines, D.; Xie, T.; Choudhary, K. Inverse Design of Next-Generation Superconductors Using Data-Driven Deep Generative Models. *J. Phys. Chem. Lett.* **2023**, *14* (29), 6630−6638.
(4) Li, J.; Cai, Q.; Horri, B. A. Highly Conductive and Stable Electrolytes for Solid Oxide Electrolysis and Fuel Cells: Fabrication, Characterisation, Recent Progress and Challenges. *Mater. Adv.* **2025**, *6*, 39−83.
(5) Fergus, J. W. Electrolytes for Solid Oxide Fuel Cells. *J. Power Sources* **2006**, *162* (1), 30−40.
(6) Jiang, J.; Hertz, J. L. On the Variability of Reported Ionic Conductivity in Nanoscale YSZ Thin Films. *J. Electroceram.* **2014**, *32* (1), 37−46.
(7) Minh, N. Q. Ceramic Fuel Cells. *J. Am. Ceram. Soc.* **1993**, *76* (3), 563−588.
(8) Haile, S. M. Fuel Cell Materials and Components. *Acta Mater.* **2003**, *51* (19), 5981−6000.
(9) Malavasi, L.; Fisher, C. A.; Islam, M. S. Oxide-Ion and Proton Conducting Electrolyte Materials for Clean Energy Applications: Structural and Mechanistic Features. *Chem. Soc. Rev.* **2010**, *39* (11), 4370−4387.
(10) Yamamoto, O. Solid Oxide Fuel Cells: Fundamental Aspects and Prospects. *Electrochim. Acta* **2000**, *45* (15−16), 2423−2435.
(11) Stambouli, A. B.; Traversa, E. Solid Oxide Fuel Cells (SOFCs): A Review of an Environmentally Clean and Efficient Source of Energy. *Renew. Sustain. Energy Rev.* **2002**, *6* (5), 433−455.
(12) Lee, H. B.; Prinz, F. B.; Cai, W. Atomistic Simulations of Surface Segregation of Defects in Solid Oxide Electrolytes. *Acta Mater.* **2010**, *58* (6), 2197−2206.
(13) Madhual, S.; Kumar, P. P. Insights on Oxide Ion Transport in Yttria-Doped Ceria from Molecular Dynamics Simulations. *J. Mater. Sci.* **2023**, *58* (10), 4499−4512.
(14) Tarancón, A.; Morata, A.; Peiró, F.; Dezanneau, G. A Molecular Dynamics Study on the Oxygen Diffusion in Doped Fluorites: The Effect of the Dopant Distribution. *Fuel Cells* **2011**, *11* (1), 26−37.
(15) Hein, P.; Grope, B. O.; Koettgen, J.; Grieshammer, S.; Martin, M. Kinetic Monte Carlo Simulations of Ionic Conductivity in Oxygen Ion Conductors. *Mater. Chem. Phys.* **2021**, *257*, 123767.
(16) Koettgen, J.; Grieshammer, S.; Hein, P.; Grope, B. O.; Nakayama, M.; Martin, M. Understanding the Ionic Conductivity Maximum in Doped Ceria: Trapping and Blocking. *Phys. Chem. Chem. Phys.* **2018**, *20* (21), 14291−14321.
(17) Tada, T.; Watanabe, N. Parallelized Meso-Scale Kinetic Monte Carlo Simulations for Sofc Characterization. *ECS Trans.* **2013**, *57* (1), 2437.
(18) Tada, T. Full Atomistic Kinetic Monte Carlo and First Principles Study on Electromotive Force of SOFC with Direct Counting Approach. *ECS Trans.* **2017**, *78* (1), 2815.
(19) Nakata, H.; Araidai, M.; Bai, S.; Hirano, H.; Tada, T. Accurate Meso-Scale Dynamics by Kinetic Monte Carlo Simulation via Free Energy Multicanonical Sampling: Oxygen Vacancy Diffusion in $BaTiO_3$. *Sci. Technol. Adv. Mater. Methods* **2021**, *1* (1), 109−122.
(20) Jansen, A. P. J. *An Introduction to Kinetic Monte Carlo Simulations of Surface Reactions*; Springer, 2012; Vol. *856*.
(21) Pornprasertsuk, R.; Cheng, J.; Huang, H.; Prinz, F. B. Electrochemical Impedance Analysis of Solid Oxide Fuel Cell Electrolyte Using Kinetic Monte Carlo Technique. *Solid State Ion* **2007**, *178* (3−4), 195−205.
(22) Hoffmann, M. J.; Bligaard, T. A Lattice Kinetic Monte Carlo Solver for First-Principles Microkinetic Trend Studies. *J. Chem. Theory Comput.* **2018**, *14* (3), 1583−1593.
(23) Strickler, D. W.; Carlson, W. G. Ionic Conductivity of Cubic Solid Solutions in the System CaO—Y_2 O_3 —ZrO_2. *J. Am. Ceram. Soc.* **1964**, *47* (3), 122−127.
(24) Thorp, J. S.; Buckley, H. P. The Dielectric Constants of Current-Blackened Single Crystral Yttria-Stabilized Zirconia. *J. Mater. Sci.* **1973**, *8* (10), 1401−1408.
(25) Pornprasertsuk, R.; Ramanarayanan, P.; Musgrave, C. B.; Prinz, F. B. Predicting Ionic Conductivity of Solid Oxide Fuel Cell Electrolyte from First Principles. *J. Appl. Phys.* **2005**, *98* (10), 103513.
(26) Grieshammer, S.; Eisele, S.; Koettgen, J. Modeling Oxygen Ion Migration in the CeO_2 − ZrO_2 − Y_2 O_3 Solid Solution. *J. Phys. Chem. C* **2018**, *122* (33), 18809−18817.
(27) Sklearn. Feature_selection. VarianceThreshold. https://scikit-learn.org/stable/modules/generated/sklearn.feature_selection.VarianceThreshold.html (accessed Sep 3, 2025).
(28) tsfresh. https://tsfresh.readthedocs.io/ (accessed Dec 7, 2024).
(29) scikit-learn. https://scikit-learn.org/ (accessed May 30, 2024).
(30) Yamahara, K.; Jacobson, C. P.; Visco, S. J.; De Jonghe, L. C. Influence of Powders on Ionic Conductivity of Polycrystalline Zirconias. *ECS Proc.* **2003**, *2003* (1), 187.
(31) Lee, E.; Prinz, F. B.; Cai, W. Enhancing Ionic Conductivity of Bulk Single-Crystal Yttria-Stabilized Zirconia by Tailoring Dopant Distribution. *Phys. Rev. B* **2011**, *83*, 052301.

Downloaded from pubs.acs.org/jpccck/article-pdf/130/10/3897/6422852/jp5c06852.pdf by NATL INST FOR MATLS SCIENCE (NIMS) user on 15 September 2026

https://doi.org/10.1021/acs.jpcc.5c06852
J. Phys. Chem. C 2026, 130, 3897−3908